

The Stationary Point: A New Method for Solar Wind Speed Measurements from a Moving Vantage Point

SAMUEL J. VAN KOOTEN,¹ CRAIG E. DEFOREST,¹ GUILLERMO STENBORG,² AND KENNY N. KENNY^{3,1}

¹*Southwest Research Institute, 1301 Walnut St. Suite 400, Boulder CO 80302*

²*The Johns Hopkins University Applied Physics Laboratory, Laurel, MD 20723, USA*

³*University of Colorado, Boulder, Department of Astrophysical and Planetary Sciences
2000 Colorado Ave, Boulder, CO 80305, USA*

(Received September 30, 2024; Revised January 17, 2025; Accepted February 1, 2025)

Submitted to ApJ

ABSTRACT

The WISPR imager on Parker Solar Probe provides a unique view the young solar wind, flying through solar wind structures at high speed. It is of interest to use WISPR image sequences to measure the velocity of both large features (such as CMEs) and the background, ambient wind. However, WISPR's close-up, rapidly-moving perspective makes the usual methods for measuring velocities from images difficult or impossible to apply, as most apparent motion through the image is due to the motion or rotation of the imager. In this work, we propose a new method of looking for features at the “stationary point”—a direction from which some plasma parcels appear to approach the spacecraft, remaining at a constant direction in the image sequence. This direction is a function of the plasma’s radial velocity, the encounter geometry, and the spacecraft velocity, allowing the former two to be inferred. We demonstrate the technique with forward-modeled images, and we apply it to WISPR observations, inferring the speed and trajectory of a particular density feature. This method promises to enable speed measurements of the young solar wind in an important acceleration region, from a close-up perspective and at latitudes well outside the PSP orbital plane. And while we present this method in a solar wind context, it is broadly applicable to any situation of a moving viewpoint traveling through an expanding cloud of features.

Keywords: Solar wind (1534); Solar corona (1483); Solar coronal transients (312)

1. INTRODUCTION

The solar wind is a continual outflow of heated plasma from the Sun which fills the heliosphere, and the cause of its acceleration is an open question of great interest in the field (Viall & Borovsky 2020) for which many competing mechanisms have been proposed (see, e.g., discussions in Cranmer et al. 2017; Cranmer & Winebarger 2019). The main difficulty in resolving the question is the lack of strong observational constraints that are able to differentiate between the proposed mechanisms (though recent observations have shed new light, e.g. Bale et al. 2023). One type of observation that can con-

tribute is a measurement of solar wind flow speeds at a range of distances from the Sun, as this will constrain where and to what degree acceleration is occurring. To this end, we propose a new method for measuring wind flow speeds with the Wide-field Imager for Parker Solar Probe (WISPR; Vourlidas et al. 2016) imager on board Parker Solar Probe (PSP; Fox et al. 2016). PSP’s extreme proximity to the Sun ($\sim 10 R_{\odot}$ near perihelion in the latter portion of the planned mission) and WISPR’s field of view reaching to within 13° of the Sun allow WISPR to probe the solar wind very close to the Sun—as low as a few R_{\odot} —in a region where the majority of the wind’s acceleration has been seen to occur (e.g. Wexler et al. 2020).

It has long been known that inhomogeneities pervade the outer corona and the young solar wind (e.g. Sheeley et al. 1997; Viall & Vourlidas 2015; DeForest et al. 2018),

providing visual tracers of the wind’s motion, and tracking these density features allows a remote measurement of the wind’s speed. Such tracking applied to WISPR requires new or adapted techniques, as traditional methods of flow tracking and speed inference are difficult or impossible to apply. This is due primarily to PSP’s rapid motion and close proximity to the young solar wind, as well as the constant rotation of WISPR’s field of view (as PSP rotates to maintain heat shield alignment). These effects mean that the true motion of a feature of interest drives only a portion of its motion through the image plane, with parallax and field-of-view rotation causing the remainder. We therefore develop a new technique, in which a feature’s apparent motion through the image plane, combined with a full consideration of the observing geometry, allows a feature’s speed and trajectory to be inferred. While developed for WISPR, this technique is in no way limited to this one application, but could be used in similar situations in which one’s viewpoint is moving steadily through a cloud of radially-expanding features.

Other successful efforts to extract plasma positions and velocities from WISPR images exist. Liewer et al. (2019, 2020) developed a technique for determining the trajectory of density features in WISPR images that make use of PSP’s rapid motion near perihelion. Using the multiple views of the feature over several hours, its direction and velocity can be found by tracking the feature’s changing location in the images and fitting this sequence with an analytic expression relating image-plane motion to motion in a heliocentric coordinate frame. A modification of this technique (Liewer et al. 2022, 2023) can be used to determine the coordinates of ray-like features by tracking points distributed along the ray over the course of a few hours and again fitting the motion to the analytic expressions. A method proposed by Kenny et al. (2023) will extract the locations of ray-like structures which pass over or under WISPR by using only the apparent motion of the ray through the image plane. This technique promises to easily scale to track all rays seen by WISPR. When a feature can be identified with WISPR and another imager at a different location, its location can be triangulated from these separate viewpoints (Liewer et al. 2021). (Such triangulation applied in solar physics dates back at least as far as the early days of the Solar TERrestrial RELations Observatory mission; Thompson 2009.) Similarly, Braga & Vourlidas (2021) extended the method of Liewer et al. (2020) to use a second viewpoint, allowing them to relax the assumption that the feature is moving radially at constant velocity. As a final example, Nisticò et al. (2020) explore the use of feature brightness to allow features to

be located solely from WISPR observations. The feature’s distance from the Sun and its location relative to the Thomson sphere affect its observed brightness, so the observed variation of brightness with time adds additional information that can be fit alongside the feature’s observed elongation to determine its location and speed.

In this paper, we introduce our method, which we call the “stationary point method.” We develop the approach in three phases, considering first the case of PSP moving in a straight line at constant velocity, with plasma features in the orbital plane. We extend to a realistic PSP trajectory, and then we build further to the 3D case, where the plasma being observed is outside the orbital plane. Each stage is demonstrated with synthetic images from a forward model. Having shown that speeds and trajectories can be accurately inferred in the 3D case, we next apply the method to a real plasma feature seen by WISPR, demonstrating its viability in the real world. We leave to planned future work the task of measuring many such features across the WISPR data catalog.

2. THE STATIONARY POINT METHOD

2.1. *Introduction by analogy*

The *stationary point* concept can be introduced quickly by analogy to driving a car during a snow storm (a familiar situation for some readers—and these authors). While the snow is falling downward, the car’s forward velocity makes it appear in the car’s reference frame that the snow is traveling with some horizontal velocity (the negative of the car’s velocity), and the snow appears to approach the car from a direction somewhere between horizontal and vertical. If the car speeds up, the snow’s apparent approach direction becomes closer to horizontal. If the car stops, the snow appears to the driver to be falling vertically. If the car maintains its speed but the snow’s (true) vertical velocity were somehow increased significantly, its apparent approach direction would be closer to vertical. It is clear that this apparent approach direction is a function of the snow’s velocity, the car’s velocity, and the geometry of the situation (i.e. the snow is falling down with a uniform velocity, and the car is maintaining straight, horizontal motion). Since the latter two are known by the driver, a measurement of this approach direction can allow the snow’s velocity to be inferred.

This concept applies just as well to PSP flying through a cloud of radially-outflowing density enhancements in the solar wind. We focus specifically on those density features which eventually collide with the spacecraft (or

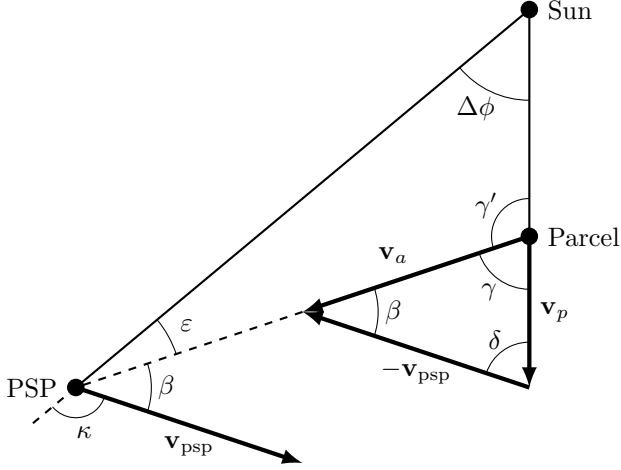


Figure 1. Diagram of stationary point geometry.

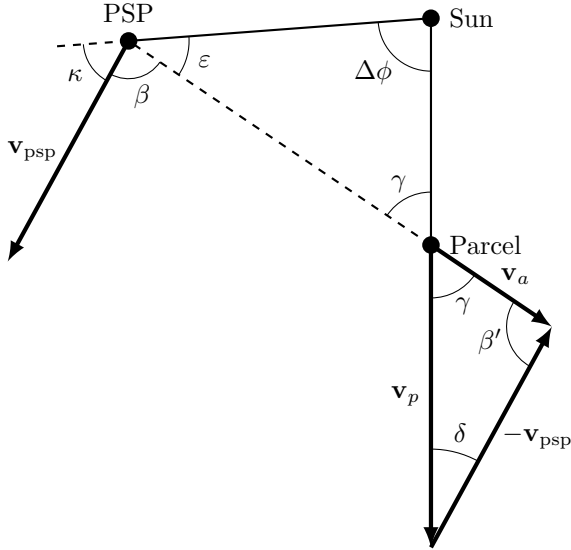


Figure 2. Alternative geometry for the case in which the parcel is growing more distant from the spacecraft.

rather, through which the spacecraft travels) or which pass directly over or under PSP.

2.2. Straight-line spacecraft motion

2.2.1. Geometry

In a first, simplified case in which PSP is traveling in a straight line with a constant velocity and the plasma being observed is in the orbital plane, collision-course plasma parcels appear to approach PSP from a fixed direction, because in PSP’s rest frame such parcels are directly approaching PPS, and therefore the parcels remain on the same line of sight and appear at the same position in the WISPR image plane throughout their approach. This is the origin of the term “stationary point,” referring to the angular position at which these parcels

appear stationary (though growing larger)—as opposed to the majority of parcels, on non-collision-course trajectories, which move in apparent position in the imaging plane. An alternative case is also possible, in which the parcel is growing more distant along the line of sight, rather than approaching PSP. This corresponds to a parcel which previously “collided” with PSP (from behind, if it is now being observed by the forward-facing camera), and such parcels also appear at a constant angular position.

We develop this geometry further with the aid of Figures 1 and 2 for the “parcel approaching” and “parcel retreating” cases, respectively, focusing first on the “approaching” case. A plasma parcel moves radially out from the Sun at constant velocity v_p , and PSP moves in a straight line at constant velocity v_{psp} . In the spacecraft frame of reference, PSP is stationary and the parcel moves with an apparent velocity $\mathbf{v}_a = \mathbf{v}_p - \mathbf{v}_{\text{psp}}$. In the two cases shown, \mathbf{v}_a is pointed directly toward or away from PSP, indicating a future or past collision, and also indicating the parcel will always be seen in the same direction—that of the stationary point, a constant angle β relative to the forward direction of the spacecraft (defined as the angle between \mathbf{v}_{psp} and \mathbf{v}_a ’s continuation to PSP—the latter vector is equivalent to the line of sight along which the parcel is seen).

We also mark β where it appears again in the triangle of velocity vectors as well as the angles ϵ , the elongation from the Sun at which the parcel is seen; κ , the angle between \mathbf{v}_{psp} and the continuation of the Sun–PSP line; $\Delta\phi$, the longitudinal separation between the parcel and PSP; δ , the angle between \mathbf{v}_p and \mathbf{v}_{psp} ; γ , the angle between \mathbf{v}_p and \mathbf{v}_a ; $\gamma' = 180^\circ - \gamma$, and $\beta' = 180^\circ - \beta$. Some of these angles will not be used until Section 2.4.

To produce an expression relating the stationary point location to the plasma velocity, we look at the Sun–parcel–spacecraft triangle in Figure 1 and write

$$180^\circ = (180^\circ - \gamma) + \epsilon + \Delta\phi \quad (1)$$

$$\Rightarrow \gamma = \epsilon + \Delta\phi. \quad (2)$$

In the triangle created by the parcel’s velocity vectors, we use the law of sines:

$$\frac{v_{\text{psp}}}{\sin \gamma} = \frac{v_p}{\sin \beta} \quad (3)$$

$$v_p = \frac{v_{\text{psp}} \sin \beta}{\sin(\epsilon + \Delta\phi)} \quad (4)$$

This contains $\Delta\phi$, the longitudinal separation between spacecraft and parcel, which is not known. However, this can be simplified by considering for now only the moments just before or just after collision, illustrated in Figure 3, when the longitudinal separation between the

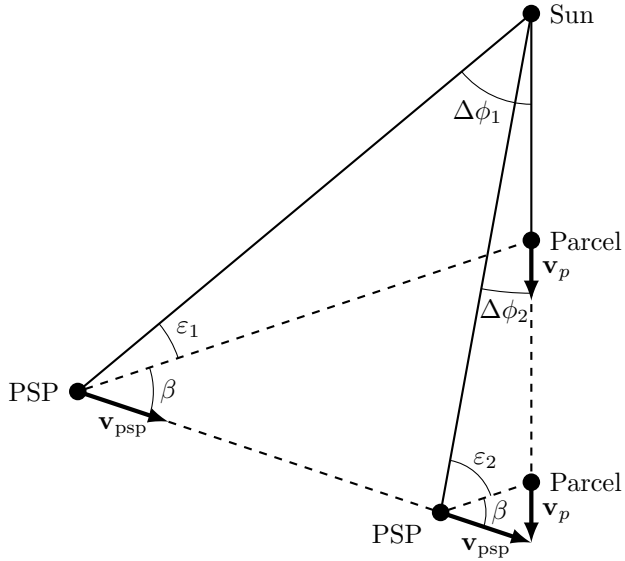


Figure 3. The situation just before collision. Shown are the same PSP and parcel positions as in Figure 1, as well as later positions when the two are much closer together. β is the same across the two cases by the nature of the “collision course” geometry, but ε has increased and $\Delta\phi$ has decreased.

parcel and PSP approaches zero and therefore $\Delta\phi \ll \varepsilon$, so

$$v_p = v_{\text{psp}} \frac{\sin \beta}{\sin \varepsilon}. \quad (5)$$

In these moments immediately before or after collision, the parcel velocity can thus be determined from the known spacecraft velocity and the stationary point’s measured location measured relative to two reference points: the Sun (for ε) and the spacecraft’s velocity direction (for β). The latter direction is fixed in this scenario, and so β can be converted from an angle relative to any other convenient reference direction—for example, the center point of the camera field of view.

For the “parcel retreating” case of Figure 2, (i.e. \mathbf{v}_a pointing directly away from the spacecraft instead of directly toward it), in Equation 3 $\sin \beta$ becomes $\sin \beta' = \sin(180^\circ - \beta) = \sin \beta$, and the expression for $\sin \gamma$ becomes $\sin(180^\circ - \varepsilon - \Delta\phi) = \sin(\varepsilon + \Delta\phi)$, so Equations 4 and 5 are unchanged. The two cases will, however, become distinct in the 3D geometry of Section 2.4.

The division between the “parcel approaching” and “retreating” cases occurs when $\Delta\phi$ is such that \mathbf{v}_p is parallel to \mathbf{v}_{psp} . In this case, for the parcel to remain on the same line of sight, the two velocities—which match in direction—must also match in magnitude, and so the plasma parcel is at a fixed location in the spacecraft frame, neither approaching nor retreating from PSP. This dividing value is $\Delta\phi = \kappa$, where $\kappa = 180^\circ - \beta - \varepsilon$. For $\Delta\phi < \kappa$, \mathbf{v}_p has a component toward PSP, and for

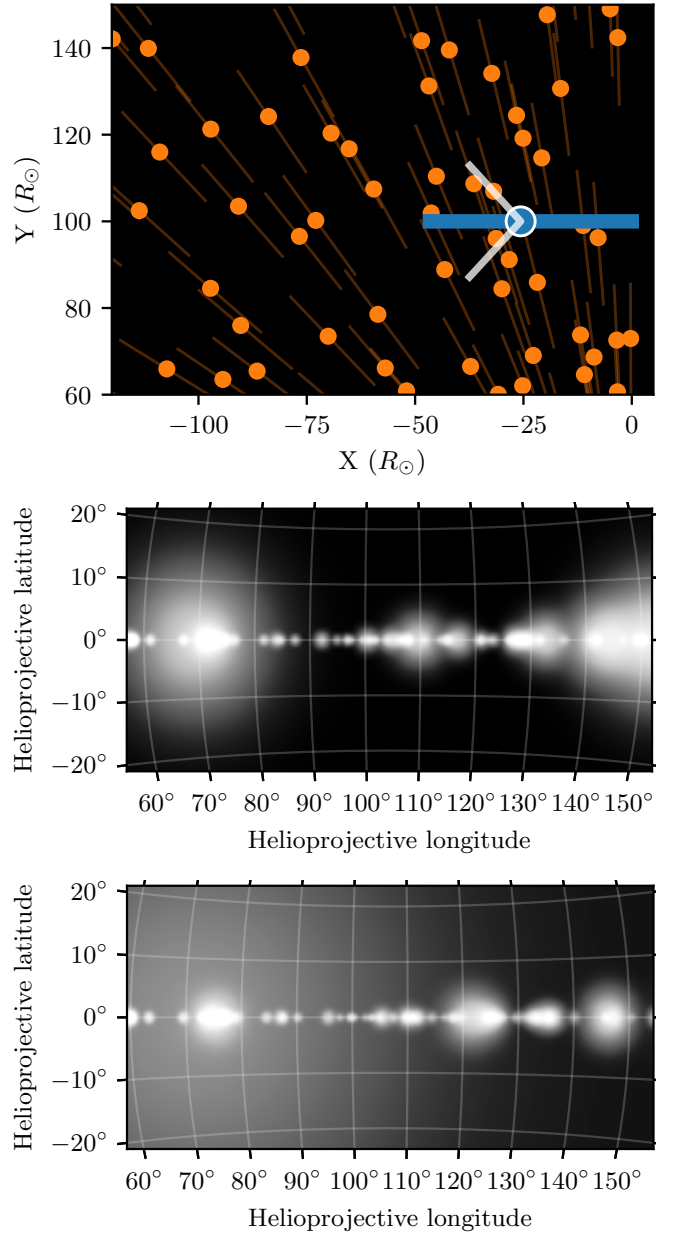


Figure 4. Top: an overhead view of our model setup, with the spacecraft (blue dot) traveling to the left in a straight line (blue) and its field of view indicated by the thin white lines. A number of plasma parcels (orange) travel radially out from the Sun, with their positions over the entire time range indicated by orange lines. Center and bottom: two sample synthesized images from this model, at the same point in time as the top panel and a short time later. Of note is a large parcel on the left, which is rapidly growing in the field of view as it approaches the spacecraft on a collision course. (The left edge of the images corresponds to the bottom portion of the marked field of view.)

$\Delta\phi > \kappa$ it has a component away from PSP, making these two regimes the “approaching” and “retreating” cases, respectively.

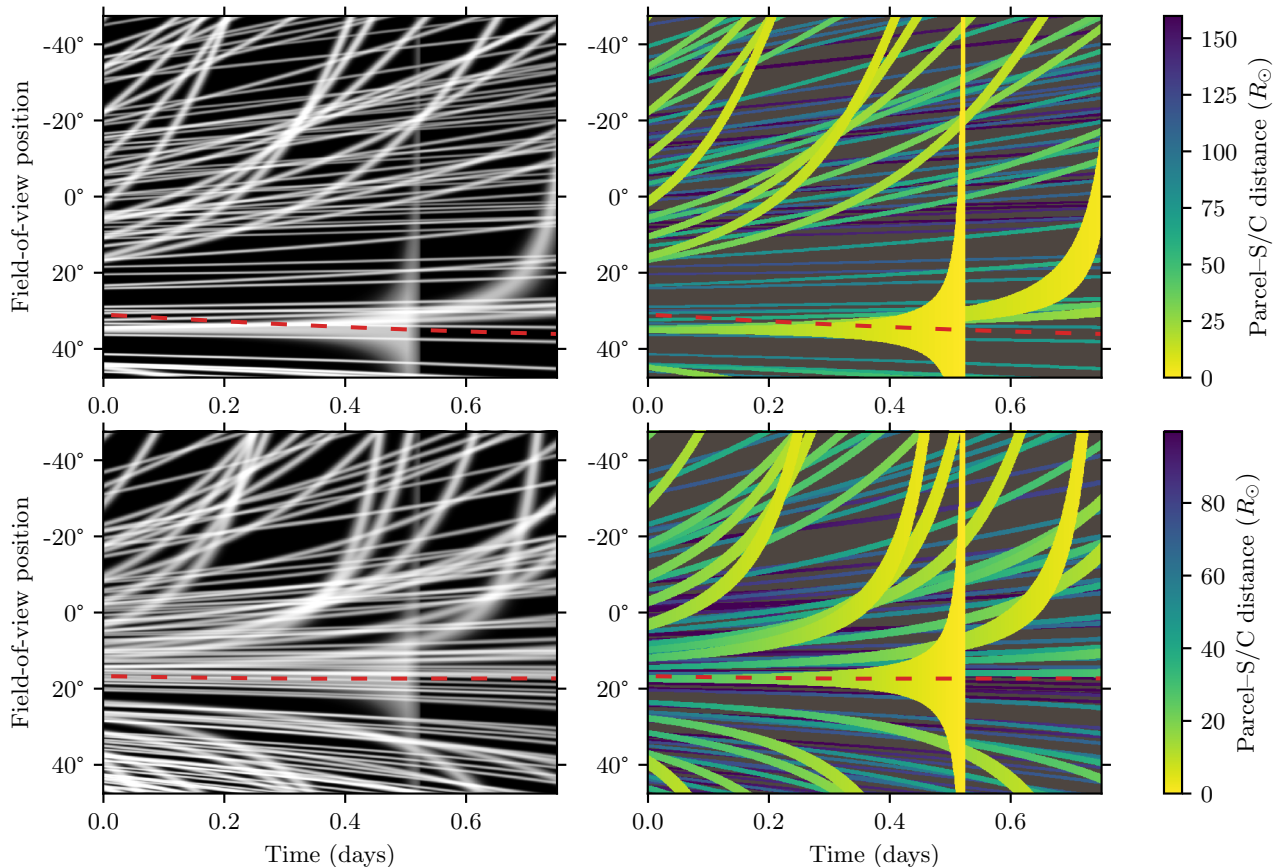


Figure 5. Synthetic time–distance plots produced by straight-line spacecraft motion through a cloud of plasma parcels (as shown in Figure 4). The parcels move radially-out from the Sun at 300 km s^{-1} (top) or 150 km s^{-1} (bottom) and the spacecraft moves at 500 km s^{-1} . The left column shows simulated white-light flux, while the right column shows the distance from the spacecraft to the nearest parcel along each line of sight, to illustrate which parcels are passing close to the spacecraft. The red dashed line in each plot shows the expected stationary point position for a hypothetical parcel colliding with PSP at that moment, as given by Equation 5. Field-of-view position is along the 0° latitude line of Figure 4 and corresponds to β in Equation 5, with positive values closer to the Sun.

2.2.2. Model demonstration

We demonstrate the stationary-point phenomenon with a model of a spacecraft flying in a straight line through a cloud of plasma parcels, shown in a top-down view in Figure 4. A number of spherical plasma parcels of uniform size travel radially-out from the Sun, all at the same constant speed, in random directions and with random release times. For clarity and expediency, these parcels only exist in the spacecraft orbital plane (corresponding to the plane of Figure 1).

From this setup we synthesize images by casting rays from each image pixel and summing the flux contributions of each parcel the rays intersect, assuming each parcel has an intensity profile that is Gaussian with respect to the impact parameter, and imposing a $1/r^2$ falloff with the Sun–parcel distance, as well as the effects of expansion with increasing r and white-light Thomson scattering (though what is important here is the geometry of where a parcel is seen, not how bright it is). Two

sample images are shown in Figure 4. We then generate time–distance plots (sometimes called “J-maps”), shown in Figure 5 for two different plasma velocities (i.e., two different model runs). We also show plots indicating the distance to each feature seen in the time–distance plots, to aid in discriminating foreground and background objects. The time–distance plots represent a single strip extracted from each image and stacked to produce the *time* axis. The strip we extract is along the projection into the image plane of the plane containing the plasma parcels, the Sun and the spacecraft. (This projection may in principle be curved, depending on the camera pointing and projection.) In this case, the strip is the line of 0° latitude, and the *distance* axis of the time–distance plots therefore represents horizontal position in the image plane. This emphasis on slicing along the projected orbital plane, as opposed to simply taking an arbitrary row of pixels (though in this simple example the projected plane is in fact a row of pixels), is because

parcels in the orbital plane remain on this strip through the entire image sequence, whereas parcels outside the orbital plane move in two dimensions through the image plane and therefore cannot be represented on a time–distance plot with a single *distance* axis. This will become important in Section 2.3, when the projected plane is no longer a straight line, and this restriction will be lifted in Section 2.4.

It is readily apparent in these time–distance plots that there is a small range of field-of-view positions at which we see horizontal motion paths, indicating a feature remaining at a fixed angular position in the field of view, and it is this location that we call the stationary point. Other streaks tend to curve away from the stationary point. The apparent stationary point location aligns well with the expected location given by Equation 5, indicated by the dashed red lines in each plot (which we compute with knowledge of v_p for this simulation). These lines indicate where a hypothetical plasma parcel would appear if it were just about to collide with PSP at that moment (and so the $\Delta\phi \ll \varepsilon$ approximation is valid). The expected stationary point location varies with time—this reflects the changing location of the Sun relative to PSP, which affects the approach direction of the radial-out plasma parcels and changes the relationship between β and ε , both of which appear in Equation 5. (Recall that the parcel appears at a fixed β , a constant angle relative to the fixed PSP velocity direction, whereas ε is that same angle measured relative to a *variable* reference point, the direction to the Sun.)

Each model run includes one parcel placed to collide exactly with the spacecraft at approximately 0.55 days. This parcel is seen to approach from a fixed direction (being $\beta = 35^\circ, 17^\circ$; $\varepsilon = 73^\circ, 91^\circ$ at collision for the upper and lower rows of Figure 5, respectively) and steadily grow larger and larger, before filling the field of view as it washes over the spacecraft.

By comparison with the distance maps also in Figure 5, we see that the streaks which curve significantly correspond to parcels passing very close to the spacecraft. These are “near-miss” parcels—ones which do not collide with the spacecraft, but get very close to doing so. When they are further away, they appear almost identical to true collision-course parcels and approach the spacecraft from a constant angular position very close to the stationary point. But as they approach and then miss the spacecraft, they are seen at a rapidly-changing angular position as they move from in front of the spacecraft to the side.

Comparing the expected and observed stationary points across these plots reveals a few insights. First, the stationary point location varies as the parcel ve-

locity (the wind speed) varies between the two rows of Figure 5, showing how a measurement of the observed stationary point location can be used to measure the parcel velocity. Second, as mentioned earlier, it can be seen that the expected stationary point location varies slightly with time, due to the changing relationship between ε and β . Third, in some cases (particularly the exact-collision parcel in the top row), some parcels that appear stationary and which coincide with the expected stationary point when they are close to the spacecraft are further from the expected stationary point when they are more distant. This is again because the expected stationary point location varies with time. If we had full knowledge of $\Delta\phi(t)$ for a given parcel (which we do not, with real observations), plotting the expected stationary point with time for that parcel using Equation 4 would produce a horizontal line to match the observed horizontal motion track (that is, the constant β that characterizes this “collision course” encounter).

It is important to note that in this example, there is a single stationary point (though with slight variation with time) because all the plasma parcels move with uniform velocity. If there were a distribution of plasma velocities, there would be a corresponding range of stationary point locations, one corresponding to each actual plasma velocity, which would complicate observational determination of the stationary point from a time–distance plot.

2.3. Realistic spacecraft motion

We now advance to a more realistic case, in which our model spacecraft follows the trajectory of PSP (specifically, during Encounter 13). This model setup is shown in Figure 6. In this setup, the model camera is pointed the same as WISPR: at a fixed elongation relative to the Sun. (The fixed, Sun-relative pointing is driven entirely by the spacecraft orientation, which maintains very careful heat shield alignment throughout each encounter.) In the synthesized image shown in Figure 6, it can be seen that the plasma parcels, which are placed only in the orbital plane, follow a line that is tilted slightly relative to the helioprojective equator—this is due to the inclination of the PSP orbital plane, and we again slice along the projected orbital plane when building our time–distance plots.

This realistic case adds two complications over the straight-line case. First, the spacecraft follows a very elliptical path with a rapidly-changing speed. Second, the camera rotates rather quickly through the entire encounter. We account for this rotation by modifying our time–distance plots so that the “distance” axis depicts the angular direction of each line of sight in a fixed ref-

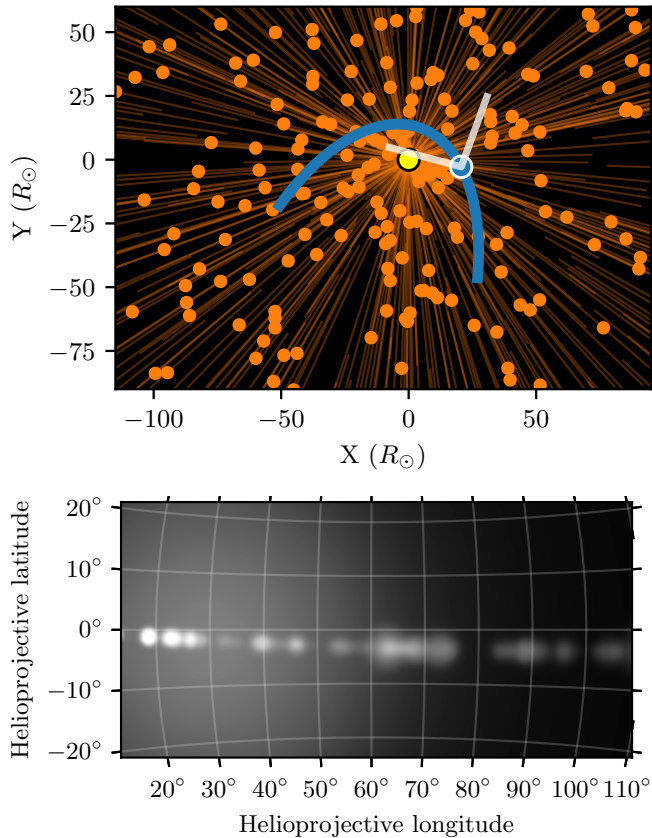


Figure 6. The same as Figure 4, but for a real PSP motion track (that of Encounter 13) and real WISPR pointing. The yellow dot marks the Sun. Note that the dots in the upper panel represent only locations, not to-scale sizes.

erence frame. In the overhead maps of Figures 4 and 6, this angle is that of a polar coordinate system centered on the spacecraft, whose origin translates but does not rotate to follow the spacecraft. (If the PSP orbital frame were aligned with the celestial equator, this angle would be identical to right ascension.) We call this presentation of the data a “de-rotated” time–distance plot, as it subtracts out the rotation of the camera. We show this in Figure 7, where we demonstrate an elongation-versus-time plot, which is simply a strip along the orbital plane taken from each image and stacked together, and our de-rotated plot, in which each column from the first image is offset according to the pointing of the camera for that image. We produce an “expected stationary point” location for each time step by approximating the spacecraft velocity at that point as constant in time and applying Equation 5. (This is analogous to breaking the full time sequence into small windows of time in which the spacecraft velocity is close to constant, and then treating each window separately.) This location will describe where parcels are expected to appear in the moments right before intercepting the spacecraft, but they

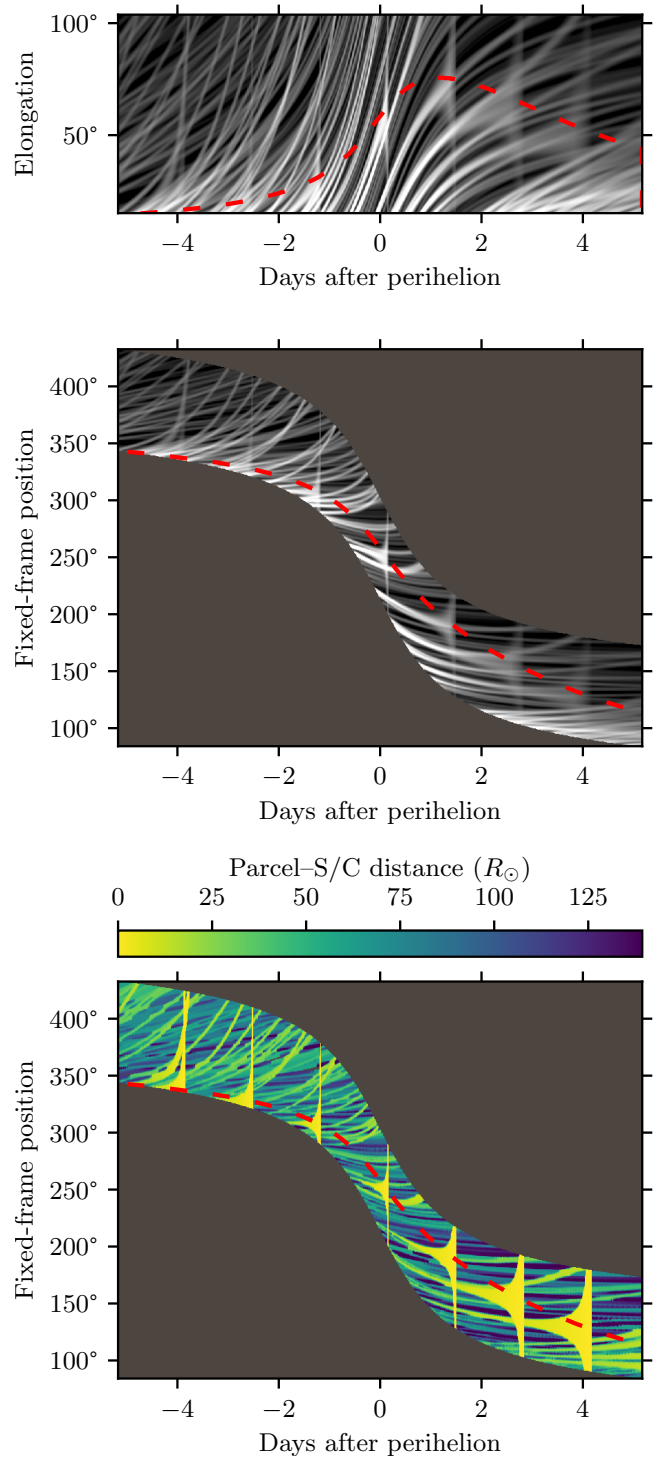


Figure 7. Time–distance plots for realistic PSP motion. Top: A traditional time–distance plot showing elongation (angular distance from the Sun). Middle: Our “de-rotated” plot, using a fixed-frame angular position as the distance axis. Bottom: A corresponding map of the distance from the spacecraft to the nearest parcel on each line of sight. The red dashed lines indicated the expected stationary point location. The uniform plasma speed is 100 km s^{-1} .

Now introducing a time dependence, we write

$$\alpha(t) = \tan^{-1} \left(\frac{d_z(t)}{d_{xy}(t)} \right), \quad (8)$$

$$d_z(t) = d_{z0} + v_{pz}t, \quad (9)$$

$$d_{xy}(t) = d_{xy0} - v_a t, \quad (10)$$

and we explore

$$\frac{d\alpha}{dt} = \frac{d}{dt} \tan^{-1} \left(\frac{d_{z0} + v_{pz}t}{d_{xy0} - v_a t} \right). \quad (11)$$

Expanding and simplifying by setting $t = 0$ (where this represents the time of our observation), we reach (after substitutions)

$$\frac{d\alpha}{dt} = \frac{v_a \tan \alpha + v_{pxy} \tan \theta}{d_{xy0} (1 + \tan^2 \alpha)}. \quad (12)$$

Substituting further using the preceding equations, we arrive at the unwieldy expression

$$\begin{aligned} \frac{d\alpha}{dt} = & \left[\pm \sqrt{v_{psp}^2 + v_{pxy}^2 + 2v_{psp}v_{pxy} \cos(\beta + \varepsilon + \Delta\phi)} \right. \\ & \cdot \frac{\tan \alpha \sin(\varepsilon + \Delta\phi)}{r_{psp} \sin \Delta\phi} \\ & \left. + \frac{v_{pxy} \tan \alpha \sin(\varepsilon + \Delta\phi)}{r_{psp} \sin \varepsilon} \right] \\ & / [1 + \tan^2 \alpha], \quad (13) \end{aligned}$$

with the \pm coming from v_a to be discussed later. This expansion shows that the two unknowns, v_{pxy} and $\Delta\phi$, are related through only the measured values of β , ε , α and $d\alpha/dt$, plus the known values of v_{psp} and r_{psp} , producing our second constraint (C_2). The intersection of C_1 and C_2 produces a solution for v_{pxy} and $\Delta\phi$, with which all the quantities in this section can be computed, producing a complete solution for the parcel's location (r_p , $\Delta\phi$ and θ) and assumed-radial velocity vector (v_p , $\Delta\phi$ and θ)

In the case in which the parcel's in-plane projection is growing more distant from the spacecraft, the in-plane geometry is that of Figure 2. As shown in Section 2.2, the first constraint is unchanged. The additional expressions in this section are similarly unchanged, since $\sin \theta = \sin(180^\circ - \theta)$, except that v_a (Equation 6) and the expanded expression in Equation 13 take the negative root rather than the positive. This produces two variants of the second constraint, with mutually-exclusive domains divided by $\Delta\phi = \kappa$ which separates the ‘‘approaching’’ and ‘‘retreating’’ cases. The ‘‘true’’ C_2 is the union of these two variants, each restricted to its own domain.

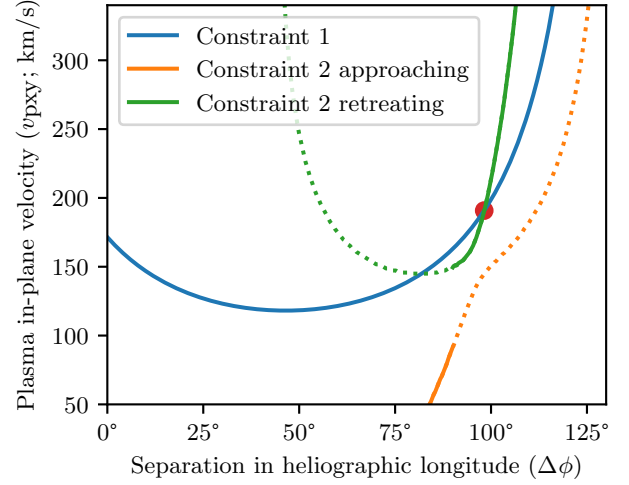


Figure 9. Constraints produced for the model setup of Figure 10. The solid portion for each of the two variants of the second constraint represent their domain of validity, and the dotted portions extend the curves outside that domain, to illustrate each more completely. The dot marks the intersection of the two constraints—a correct solution for $\Delta\phi$, v_{pxy} .

We now briefly explore the behavior of the second constraint with the aid of Figure 9, plotting C_1 and C_2 for a model setup we will present in Section 2.4.2—for now we only want an example while discussing the general behavior of C_2 . The plot shows each C_2 variant in its entirety, with the solid portions of each curve indicating each variant’s domain of validity and the ‘‘true’’ C_2 curve being the union of the two solid portions. At the dividing line of $\Delta\phi = \kappa = 180^\circ - \beta - \varepsilon$, it is clear there is a large discontinuity in this union. At this point, the δ in Equation 6 is 0. Since, as discussed in Section 2.2, $\Delta\phi = \kappa$ represents a parcel (or now its in-plane projection) moving parallel to PSP, with $v_{pxy} = v_{psp}$ in order for the parcel to stay on the same line of sight, v_a becomes zero. This allows v_a to be continuous as $\Delta\phi$ varies and crosses κ , changing the sign chosen for v_a . But this is true only when the stationary point geometry holds, with the parcel remaining at constant β . Since C_1 is an expression of that phenomenon, it essentially produces the value of v_p required for a parcel at a given $\Delta\phi$ to appear at the observed stationary point β . On the other hand, C_2 is an expression of how the out-of-plane angle α varies, and it does not overlap C_1 except at their intersection, meaning the stationary point geometry does not hold for most of the points on C_2 . This means that at $\Delta\phi = \kappa$, C_2 ’s $v_{pxy} \neq v_{psp}$, and so $v_a \neq 0$ at the sign change, producing the discontinuity we see in the plot. As the discontinuity is therefore always, if present, away from C_1 , our solution will never be at this discontinuity, while if the correct $\Delta\phi$ is κ , C_2 will cross C_1 at that

point, and so the stationary point geometry will hold and C_2 will be continuous. It is important to note that this line of thought implies that our values of C_2 are incorrect everywhere except for its intersection with C_1 (and that its valid value at the intersection is the only value we use). We derived C_2 from Equation 11, which is generally true, but we then substituted values derived from the stationary point geometry. But for a given $\Delta\phi$, the stationary point geometry requires the v_{pxy} given by C_1 , which is not the v_{pxy} given by C_2 outside the point of intersection. This means that our final expression for C_2 is valid where it intersects C_1 but inconsistent everywhere else, producing C_2 's non-physical discontinuity.

2.4.2. Model demonstration

We again demonstrate this method with our model, using the setup shown in Figure 10 containing again realistic PSP motion, but now launching parcels outside the orbital plane. This means features of interest will move throughout the image plane, so a 2D time–distance plot cannot capture these features' motion. Instead we work with a sequence of full images. As in Section 2.3, the rotation of the spacecraft must be accounted for. With the model we synthesize images with a fixed camera pointing. With data, we would reproject each image into a fixed-camera-pointing frame, thereby “de-rotating” the images. (This is discussed further in Section 3.) In both cases we align the axes of the fixed-pointing pixel grid with the orbital plane, so that horizontal pixel position is related to ε and β , and vertical pixel position is proportional to α . In the fixed-pointing or de-rotated images, we measure longitude relative to an arbitrary, fixed reference direction, meaning that it can be converted to β by subtracting an offset determined by direction of \mathbf{v}_{psp} . That offset is constant as long as the direction of \mathbf{v}_{psp} is well-approximated as constant (which it is in this model case). The elongation ε of the in-plane projection of the parcel is the fixed-pointing longitude minus the longitude of the Sun (which varies more rapidly than the offset to compute β).

In the synthesized images of Figure 10, it can be seen that a particular plasma parcel appears at a fixed longitude in the fixed-pointing images—this is a parcel at the 3D stationary point. Over the 3-hr window, in which all velocities can be approximated as constant, the other parcels can be seen to drift in longitude (which is more clear in the animated figure), whereas the stationary point parcel varies only in latitude (i.e. α). In the helio-projective images, in which the camera is pointed relative to the Sun as with WISPR, all features are seen to move through the image plane—a motion driven largely

by the rotating camera field of view (which matches the behavior of WISPR).

We click on the longitudinally-stationary parcel in 50 frames evenly spaced across our 3 hr time window, a duration chosen to match the real-data demonstration in Section 3 and which allows averaging over a number of angular measurements, and we calculate average values for β (and therefore ε) and α , and we fit a line to the time series α values to produce $d\alpha/dt$. For the time-varying quantities ε and α , these average values will represent the center of our 3 hr window, at which we consider our solution to be most valid. We compare these values to “ideal” values produced by selecting the pixel of maximum intensity in each image, and we find that clicking across many images produces average values that are accurate to within 1%. These measured values produce the constraints shown in Figure 9. From the intersection point we produce values that very closely match the input values of the model setup: the actual $\Delta\phi$ of 98° is recovered as 97.5° , the actual v_p of 194.9 km s^{-1} is recovered as 192.7 km s^{-1} , the actual θ of 12° is recovered as 11.97° , and the actual r_p of $15 R_\odot$ is recovered as $15.2 R_\odot$. (The $\Delta\phi$ and r_p values refer to the center of the 3 hr time window, and the other values are constant with time.) This demonstrates that this method can very closely recover the true values.

In addition to this case study, we have also run this full process in an automated fashion over a grid of possible parcels placed to appear at the stationary point, covering $5^\circ < \Delta\phi < 130^\circ$, $0^\circ < \theta < 75^\circ$, and $5 R_\odot < r_{\text{pxy}} < 15 R_\odot$ (with a corresponding v_p computed to place the parcel at the stationary point). The method successfully recovered the input parameters with similar accuracy across the grid. Some outlier parcels did not result in successful parameter recovery, but those were cases that, for instance, required a parcel to move radially *inward* in order to appear at the stationary point, or to travel at unrealistic speeds ($> 1000 \text{ km s}^{-1}$), outside the bounds of our numerical solution for the second constraint.

3. APPLICATION TO WISPR IMAGES

We now demonstrate the viability of this analysis on images from the WISPR imager (Vourlidis et al. 2016) on PSP. WISPR consists of a pair of white-light imagers, pointed in PSP's direction of motion with a composite field of view covering a range from 13.5° to 108° from the Sun and approximately 50° in the transverse direction. PSP travels on a highly eccentric orbit, with nominal data collection occurring while PSP is below 0.25 au on each orbit. For the data we use, from orbit 16, PSP's perihelion distance was $13.3 R_\odot$. We use approxi-

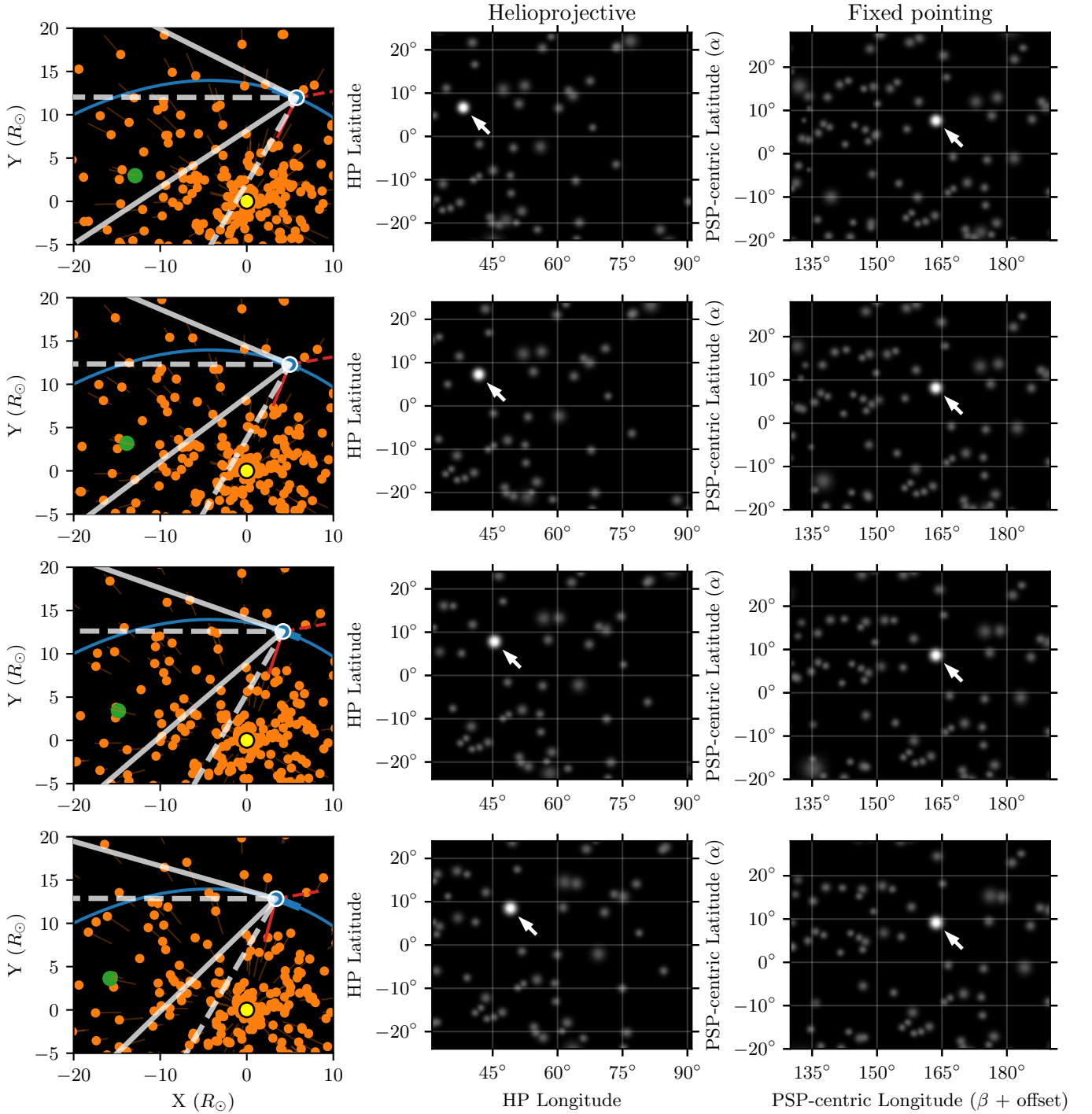


Figure 10. Model demonstration of the stationary point in 3D. The left-hand column provides an overhead view at four points in time across a 3-hr window. As in Figures 4 and 6, the blue dot and curve are the spacecraft and its trajectory, orange marks plasma parcels, and yellow marks the Sun. The solid white lines indicate a camera field-of-view with constant helioprojective pointing (which tracks the Sun’s location as WISPR does), while the dashed white lines indicate a field-of-view with a fixed direction from the spacecraft location. Red lines in the same styles mark the zero point for longitude in each frame. The center column shows images synthesized with the constant helioprojective pointing, and the right-hand column shows images with fixed-direction pointing. One parcel of interest is at the stationary point. It is indicated in the synthesized images by an arrow and by artificially increasing its brightness, and in the overhead plot by a green dot. The left edge of each synthesized image is the sunward side. (An animated version of this figure is available.)

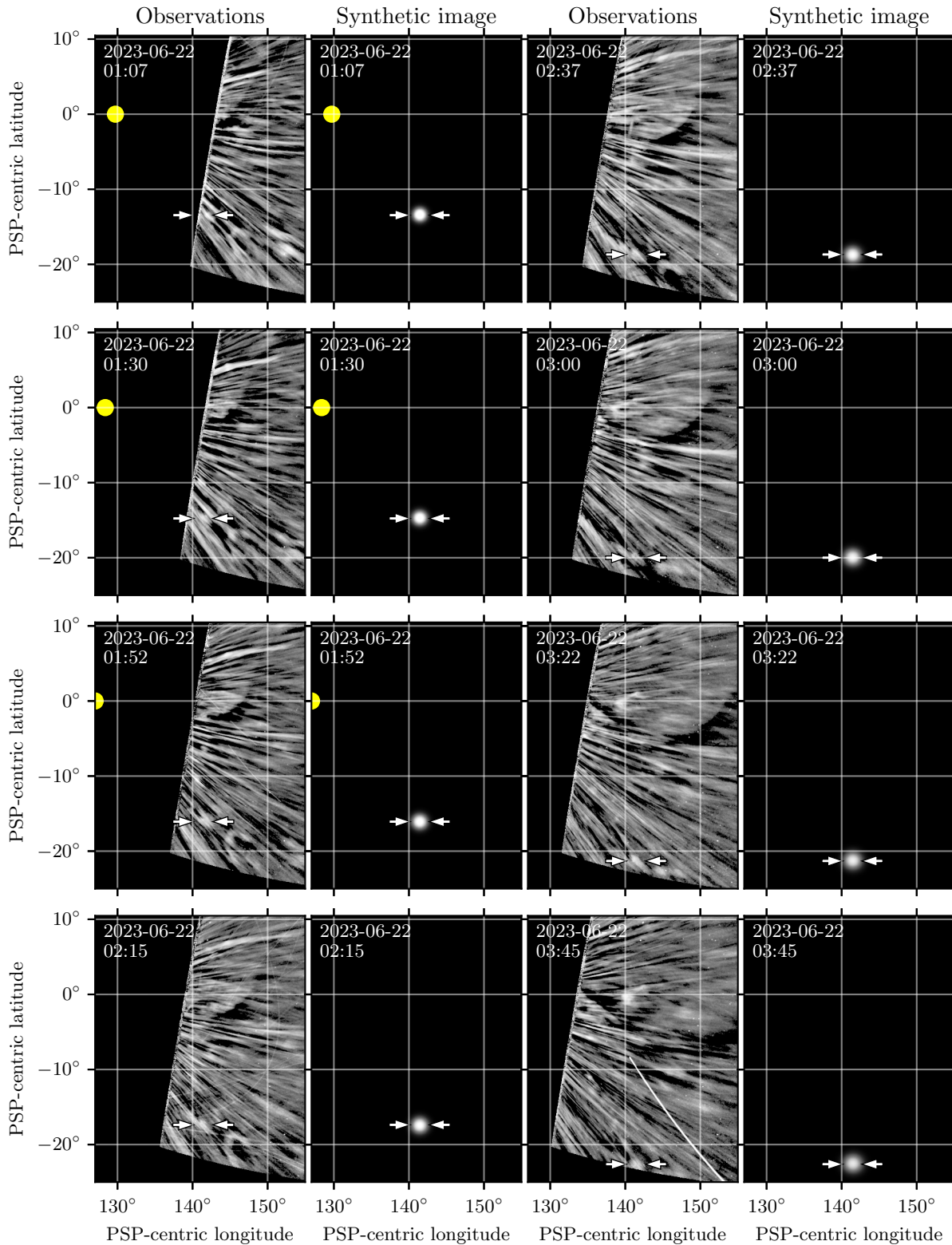


Figure 11. A sequence of images spanning 2.5 hr containing our feature of interest, marked by arrows. The first and third columns show LW-processed WISPR images, and the other columns show the feature reproduced by our forward model and the inferred parameters. The coordinate frame, described in the text, is identical for all images, and the arrows are plotted in the same location across each pair of real and synthesized images. The yellow dot marks the location of the Sun (not to scale), which is a fixed distance from the edge of the data and so quickly moves out of frame. (An animated version of this figure is available.)

mately three hours of observations near perihelion. During this time, PSP’s velocity rises from 162.4 km s^{-1} to 163.0 km s^{-1} , and its direction of motion changes by 5° , indicating that PSP can be well approximated as having a constant velocity. We use LW-processed WISPR images—this technique, described in the Appendix of Howard et al. (2022), is similar to difference imaging in that it isolates the time-variable component of an image sequence. LW processing uses a sliding window in time and a sequence of filtering steps to estimate the steady background component in any one pixel. Each image is then divided by this background to display the time-varying component in relative terms. This method does an excellent job of removing the steady F-corona, as well as the steady portion of the K-corona, from each WISPR image, leaving behind the transient plasma we wish to study. (Importantly, the plasma at the stationary point is stationary in a fixed or rotation-stabilized reference frame, but the LW processing operates with respect to variability in the *image plane*, where this plasma is *not* stationary.)

The WISPR field of view is very nearly fixed in helioprojective coordinates, or in other words, it rotates to track the Sun as PSP moves through its orbit. However, we require stabilized images in an unrotating frame, as discussed in previous sections. We therefore reproject a sequence of images into an unrotating frame which we call the “PSP-centric frame” (identical to the “fixed pointing” frame shown in the right-hand column of Figure 10) in which the PSP-centric longitude represents a direction from the spacecraft relative to an unchanging reference direction and PSP-centric latitude is measured relative to PSP’s orbital plane¹. The WISPR images pan through this reference frame over each encounter.

We identified a sample plasma parcel which appears at a fixed PSP-centric longitude and increasingly-negative latitude—meaning it is at the 3D stationary point as described in Section 2.4. We show a sequence of frames with this stationary parcel marked in Figure 11. While other features move over it and it is at times subtle, it appears consistently over 24 frames (of which 8 are shown in the figure), and it moves with a consistent $d\alpha/dt$ over this 2.5 hr period while appearing at a fixed longitude.

Over this 2.5 hr sequence, we see the parcel at a longitude of 141° , which corresponds to values of $\varepsilon = 15.6^\circ$

¹ This PSP-centric frame is a 3D helioprojective frame (centered on PSP) that is rotated about the PSP–Sun axis to align its equator with the orbital plane, and then rotated about its poles so that 0° longitude is at a fixed but arbitrary reference direction (for example, toward a chosen distant star), rather than following the location of the Sun.

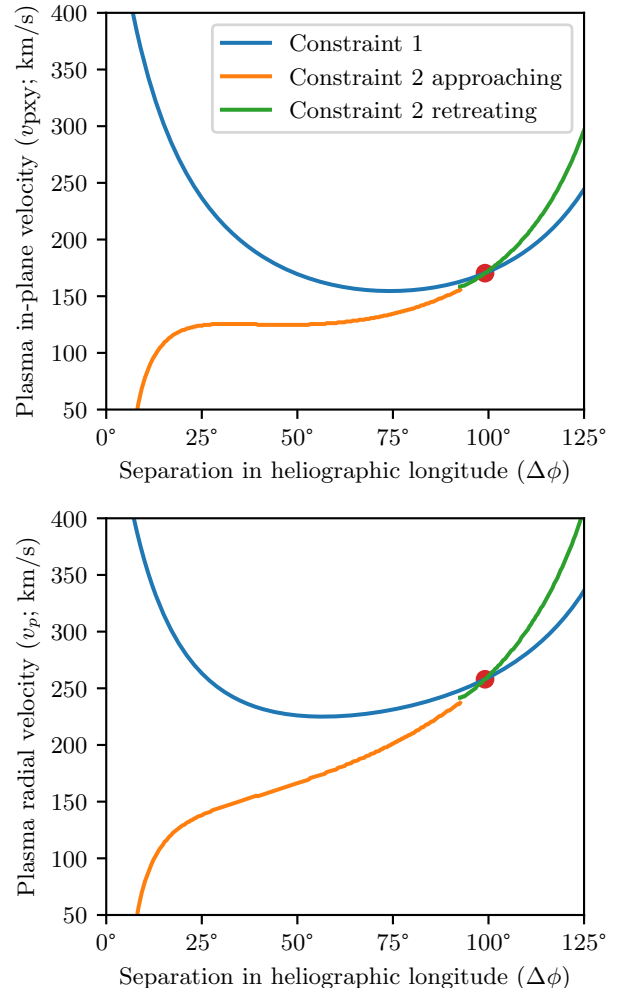


Figure 12. Constraints generated for the parcel marked in Figure 11. The two panels show in-plane speed and the corresponding total speed, respectively, with the conversion between the two being a function of θ and therefore $\Delta\phi$.

and $\beta = 71.7^\circ$ at the middle of this time window. We also measure $\alpha = -17.4^\circ$ (in the middle frame) and $d\alpha/dt = -3.5^\circ \text{ hr}^{-1}$, following the same procedure as in Section 2.4.2. By examining the resulting constraints shown in Figure 12, we infer the parcel is traveling at a velocity $v_p = 275 \text{ km s}^{-1}$, at an inclination $\theta = -49^\circ$ below PSP’s orbital plane. During this window of observations, it is about $\Delta\phi = 99^\circ$ of longitude in front of PSP. These angular coordinates correspond to a Carrington longitude of 228° and latitude of -49° . At the center of the time window, the parcel is $6.0 R_\odot$ from the Sun and $15.2 R_\odot$ from PSP. Its distance from the Sun grows from $4.4 R_\odot$ to $7.7 R_\odot$ during the 3 hr window.

Using these inferred parameters, we generate synthetic images of a parcel with the same trajectory and velocity, using the same forward model of Section 2, which are shown in the second and fourth columns of Figure 11.

It can be seen that the position of the parcel in the images is reproduced very closely, adding credibility to the claim that this parcel trajectory is implied by the observations, and that the approximations of constant spacecraft and parcel velocities are reasonable.

Our inferred values are relatively insensitive to measurement error. The measured ε , α and $d\alpha/dt$ are produced as averages or fits to marked feature locations in a number of frames, so individual “mis-clicks” will tend to balance out. (As shown in Section 2.4.2, the measured values of these angles are good to within 1% under ideal conditions.) If we allow an error of $\pm 1^\circ$ in β (and therefore ε) and α and a $\pm 5\%$ error in $d\alpha/dt$ (these are generous error margins compared to the spread of values we find after clicking the feature in each image) and compute the constraints and implied speed and trajectory across a grid of errors uniformly distributed within these ranges, we can produce a distribution of possible speeds and trajectories, which we show in Figure 13. For the feature we analyze here, the mean and standard deviation of these distributions are $v_p = 262 \pm 27 \text{ km s}^{-1}$, $\theta = -48^\circ \pm 1^\circ$, $\Delta\phi = 99^\circ \pm 11^\circ$, and $r_p = 6.1 \pm 0.5 R_\odot$, showing that the inferred values carry an uncertainty of only $\sim 10\%$ due to these assumed ranges of errors. The correlations that are seen are readily interpreted: the further away the parcel is placed (in $\Delta\phi$), the further from the Sun it must be to appear at the same angular location, and the faster it must move to produce the same angular motion.

3.1. Comparison to Other Measurements

A variety of wind speed measurements near the Sun have been reported in the literature. While there is a range of values, a few hundred km s^{-1} is typical. It is useful to compare our measured value of $271 \pm 24 \text{ km s}^{-1}$ at $6.3 R_\odot$. A variety of radio sounding observations (e.g. [Armstrong & Woo 1981](#), and references therein) span $100\text{--}225 \text{ km s}^{-1}$ at $5\text{--}10 R_\odot$. [DeForest et al. \(2018\)](#) tracked white-light features seen from Earth and made measurements of $150\text{--}175 \text{ km s}^{-1}$ at heliocentric distances as low as $7 R_\odot$. [Nindos et al. \(2021\)](#) report measurements of similar density enhancements in the solar wind seen by WISPR. By assuming all observed features are on the Thompson surface and fitting the slopes of motion tracks on time-distance plots, they report velocities of $150\text{--}300 \text{ km s}^{-1}$. In-situ measurements from PSP have recorded wind speeds from $150\text{--}500 \text{ km s}^{-1}$ at distances as low as $15 R_\odot$ ([Raouafi et al. 2023](#)). From a theoretical perspective, [Cranmer & Winebarger \(2019\)](#) illustrate that models of wind acceleration driven by anisotropic magnetohydrodynamic turbulence predict speeds at $6 R_\odot$ of up to 400 km s^{-1}

for open field lines in coronal hole regions, or as low as 150 km s^{-1} in streamers.

When comparing this range of reported values to our result, it is important to point out that we have measured a single parcel, rather than producing a distribution of measurements, meaning our result is less robust than the other values. (Reasons for this limitation and prospects for measuring additional parcels are discussed in Section 4.) Additionally, given that these reported values will use a variety of averaging methods and cover different ranges of latitude and levels of solar activity, and that Earth-bound measurements may be biased toward larger, more visible features, which may not be representative of the population of features seen by WISPR, it is difficult to directly compare our single measured parcel to any one of these studies, but it is encouraging to see that our inferred speed fits reasonably within the overall range.

4. DISCUSSION AND CONCLUSIONS

In this paper we developed a novel technique for estimating the speeds and trajectories of certain density enhancements seen by WISPR, though the technique is applicable to any moving vantage point traveling through a stream of outflowing objects. WISPR’s rapidly-moving vantage point and its close proximity to the structures being imaged are a hindrance to many flow tracking methods traditionally applied to the solar wind, but they are the tools by which this technique works. We showed that the technique can be applied despite WISPR’s sun-tracking rotation and the elliptical orbit on which it travels. We demonstrated the method by analyzing one plasma parcel seen by WISPR, producing an estimated speed and trajectory which, in turn, reproduce the observations.

Our method has several limitations, the largest of which is that only plasma features which appear at their stationary point can be measured. As shown by Equation 4, the location of the stationary point is a function of the parcel’s speed and its angular distance from the spacecraft, meaning that in any image sequence there will be a range of possible stationary points at which parcels could appear, and only those parcels that by coincidence do appear at that point (meaning that, momentarily, they are on course to “collide” with the spacecraft, or to pass directly above or below it) can be measured. The technique also can only measure parcels whose stationary point falls within the field of view. The higher the parcel speed relative to the spacecraft speed, the more Sun-ward the corresponding stationary point will be, and so the fastest parcels (which may include all parcels when the spacecraft velocity is low, far from

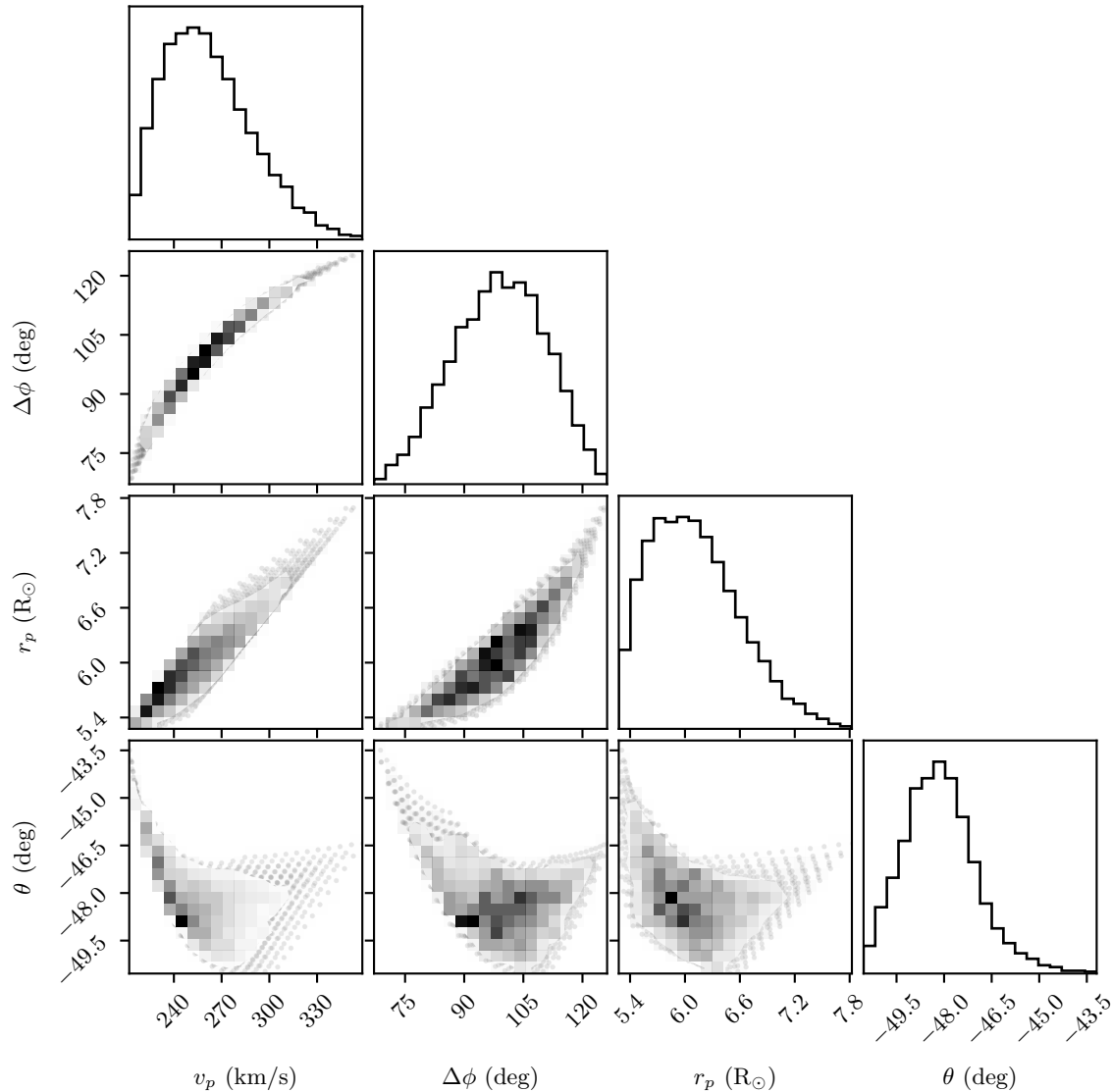


Figure 13. Distributions and correlations of output quantities over a grid of assumed errors. See the text for details.

perihelion) may not be measurable as their stationary point lies outside the field of view.

Second, we must assume that features seen at the stationary point are individual, relatively compact density enhancements moving linearly. Possible alternatives include, for instance, an elongated radial structure with a fold or perturbation (producing the observed density feature) that is propagating along the structure, or a coincidence of several unrelated, spatially disjoint, highly transitory features that appear in turn to produce the appearance of a single feature at fixed β and with a constant da/dt . Such an assumption is foundational to many wind speed measurements, but it is important to state specifically.

Third, we require a few assumptions to be valid for the velocities. The spacecraft velocity must be well-approximated as constant (in both magnitude and direc-

tion) for the period of time being analyzed, and the parcel being observed must be well-approximated as traveling radially-out from the Sun at a constant velocity during the time period. In our demonstration in Section 3, using a 3 hr window of time, these assumptions are reasonable as discussed in that section, but this may not always be the case.

Finally, addressing our science goal of constraining the speed, and therefore acceleration, of the ambient solar wind, we must assume that the discrete density features we can measure are passive tracers of the ambient wind, rather than separate, more transient features undergoing distinct physical processes.

Despite these limitations, this is a novel and useful method. The most similar method that these authors are aware of is that of [Liewer et al. \(2020\)](#), in which a feature of interest is identified in a sequence of images,

and then a parcel trajectory and speed is iteratively fit that reproduces the apparent location of the feature in the images. That method is more widely applicable, as it does not require the coincidence of the feature of interest appearing at the stationary point. (Though our limitation to a random subset of plasma parcels that appear at the stationary point may represent a convenient way of surveying a random sample of parcels relatively free of human biases.) However, our method is numerically simpler in that it does not require iterative, non-linear fitting, and so there is no concern over sensitivity to initial guesses.

In future work, we will explore the possibility of extending our method's applicability to parcels not at the stationary point by treating parcels' horizontal angular positions similarly to their vertical positions. We will also conduct a census of plasma features seen at the stationary point by WISPR and produce a catalog of inferred velocities, latitudes, etc. We expect that this will provide a sampling of wind speeds across a range of latitudes, all at close proximity to the Sun and in the critical early acceleration region.

ACKNOWLEDGMENTS

We thank M. G. Linton and P. C. Liewer for reviewing this manuscript and offering valuable suggestions. This research has made use of NASA's Astrophysics Data

System Bibliographic Services, which these authors treasure. We specifically acknowledge the Astropy/SunPy coordinate framework, which has greatly simplified a number of operations in this work. This work was supported by the NASA Parker Solar Probe Program Office for the WISPR program (NASA Contract NNG11EK11I to the U.S. Naval Research Laboratory, NRL; and NRL subcontract N00173-20-C-2002 to SwRI). Parker Solar Probe was designed, built, and is now operated by the Johns Hopkins Applied Physics Laboratory as part of NASA's Living with a Star (LWS) program (contract NNN06AA01C). Support from the LWS management and technical team has played a critical role in the success of the Parker Solar Probe mission. The Wide-Field Imager for Parker Solar Probe (WISPR) instrument was designed, built, and is now operated by the US Naval Research Laboratory in collaboration with Johns Hopkins University/Applied Physics Laboratory, California Institute of Technology/Jet Propulsion Laboratory, University of Gottingen, Germany, Centre Spatiale de Liege, Belgium and University of Toulouse/Research Institute in Astrophysics and Planetology.

Software: SunPy (SunPy Community et al. 2020) version 5.1.2 (Mumford et al. 2024), Astropy (Astropy Collaboration et al. 2013, 2018, 2022) version 6.1.0 (Astropy Collaboration 2024), Matplotlib (Hunter 2007) version 3.3.2 (Matplotlib Development Team 2024), NumPy (Harris et al. 2020) version 1.26.4, SciPy (Virtanen et al. 2020) version 1.13.0 (Gommers et al. 2024)

REFERENCES

- Armstrong, J. W., & Woo, R. 1981, *Astronomy and Astrophysics*, 103, 415
- Astropy Collaboration. 2024, *Astropy* 6.1.0, Zenodo, doi: [10.5281/zenodo.11121433](https://doi.org/10.5281/zenodo.11121433)
- Astropy Collaboration, Robitaille, T. P., Tollerud, E. J., et al. 2013, 558, A33, doi: [10.1051/0004-6361/201322068](https://doi.org/10.1051/0004-6361/201322068)
- Astropy Collaboration, Price-Whelan, A. M., Sipőcz, B. M., et al. 2018, 156, 123, doi: [10.3847/1538-3881/aabc4f](https://doi.org/10.3847/1538-3881/aabc4f)
- Astropy Collaboration, Price-Whelan, A. M., Lim, P. L., et al. 2022, 935, 167, doi: [10.3847/1538-4357/ac7c74](https://doi.org/10.3847/1538-4357/ac7c74)
- Bale, S. D., Drake, J. F., McManus, M. D., et al. 2023, *Nature*, 618, 252, doi: [10.1038/s41586-023-05955-3](https://doi.org/10.1038/s41586-023-05955-3)
- Braga, C. R., & Vourlidas, A. 2021, *Astronomy & Astrophysics*, 650, A31, doi: [10.1051/0004-6361/202039490](https://doi.org/10.1051/0004-6361/202039490)
- Cranmer, S. R., Gibson, S. E., & Riley, P. 2017, *Space Science Reviews*, 212, 1345, doi: [10.1007/s11214-017-0416-y](https://doi.org/10.1007/s11214-017-0416-y)
- Cranmer, S. R., & Winebarger, A. R. 2019, *Annual Review of Astronomy and Astrophysics*, 57, 157, doi: [10.1146/annurev-astro-091918-104416](https://doi.org/10.1146/annurev-astro-091918-104416)
- DeForest, C. E., Howard, R. A., Velli, M., Viall, N., & Vourlidas, A. 2018, *The Astrophysical Journal*, 862, 18, doi: [10.3847/1538-4357/AAC8E3](https://doi.org/10.3847/1538-4357/AAC8E3)
- Fox, N. J., Velli, M. C., Bale, S. D., et al. 2016, *Space Science Reviews*, 204, 7, doi: [10.1007/s11214-015-0211-6](https://doi.org/10.1007/s11214-015-0211-6)
- Gommers, R., Virtanen, P., Haberland, M., et al. 2024, *Scipy/Scipy: SciPy 1.13.0*, Zenodo, doi: [10.5281/zenodo.10909890](https://doi.org/10.5281/zenodo.10909890)
- Harris, C. R., Millman, K. J., van der Walt, S. J., et al. 2020, *Nature*, 585, 357, doi: [10.1038/s41586-020-2649-2](https://doi.org/10.1038/s41586-020-2649-2)
- Howard, R. A., Stenborg, G., Vourlidas, A., et al. 2022, *The Astrophysical Journal*, 936, 43, doi: [10.3847/1538-4357/ac7ff5](https://doi.org/10.3847/1538-4357/ac7ff5)
- Hunter, J. D. 2007, *Computing in Science and Engineering*, 9, 90, doi: [10.1109/MCSE.2007.55](https://doi.org/10.1109/MCSE.2007.55)

- Kenny, M. N., DeForest, C. E., West, M. J., & Liewer, P. C. 2023, *The Astrophysical Journal*, 953, 79, doi: [10.3847/1538-4357/acdfc5](https://doi.org/10.3847/1538-4357/acdfc5)
- Liewer, P., Vourlidas, A., Thernisien, A., et al. 2019, *Solar Physics*, 294, 93, doi: [10.1007/s11207-019-1489-4](https://doi.org/10.1007/s11207-019-1489-4)
- Liewer, P. C., Qiu, J., Ark, F., et al. 2022, *Solar Physics*, 297, 128, doi: [10.1007/s11207-022-02058-6](https://doi.org/10.1007/s11207-022-02058-6)
- Liewer, P. C., Qiu, J., Penteado, P., et al. 2020, *Solar Physics*, 295, 1, doi: [10.1007/s11207-020-01715-y](https://doi.org/10.1007/s11207-020-01715-y)
- Liewer, P. C., Qiu, J., Vourlidas, A., Hall, J. R., & Penteado, P. 2021, *Astronomy & Astrophysics*, 650, A32, doi: [10.1051/0004-6361/202039641](https://doi.org/10.1051/0004-6361/202039641)
- Liewer, P. C., Vourlidas, A., Stenborg, G., et al. 2023, *The Astrophysical Journal*, 948, 24, doi: [10.3847/1538-4357/acc8c7](https://doi.org/10.3847/1538-4357/acc8c7)
- Matplotlib Development Team. 2024, *Matplotlib 3.8.4*, Zenodo, doi: [10.5281/zenodo.10916799](https://doi.org/10.5281/zenodo.10916799)
- Mumford, S. J., Freij, N., Stansby, D., et al. 2024, *SunPy 5.1.2*, Zenodo, doi: [10.5281/zenodo.10927245](https://doi.org/10.5281/zenodo.10927245)
- Nindos, A., Patsourakos, S., Vourlidas, A., et al. 2021, *Astronomy & Astrophysics*, 650, A30, doi: [10.1051/0004-6361/202039414](https://doi.org/10.1051/0004-6361/202039414)
- Nisticò, G., Bothmer, V., Vourlidas, A., et al. 2020, *Solar Physics*, 295, 63, doi: [10.1007/s11207-020-01626-y](https://doi.org/10.1007/s11207-020-01626-y)
- Raouafi, N. E., Stenborg, G., Seaton, D. B., et al. 2023, *The Astrophysical Journal*, 945, 28, doi: [10.3847/1538-4357/acaf6c](https://doi.org/10.3847/1538-4357/acaf6c)
- Sheeley, N. R., Wang, Y. M., Hawley, S. H., et al. 1997, *The Astrophysical Journal*, 484, 472, doi: [10.1086/304338](https://doi.org/10.1086/304338)
- SunPy Community, Barnes, W. T., Bobra, M. G., et al. 2020, *The Astrophysical Journal*, 890, 68, doi: [10.3847/1538-4357/ab4f7a](https://doi.org/10.3847/1538-4357/ab4f7a)
- Thompson, W. T. 2009, *Icarus*, 200, 351, doi: [10.1016/j.icarus.2008.12.011](https://doi.org/10.1016/j.icarus.2008.12.011)
- Viall, N. M., & Borovsky, J. E. 2020, *Journal of Geophysical Research: Space Physics*, 125, e2018JA026005, doi: [10.1029/2018JA026005](https://doi.org/10.1029/2018JA026005)
- Viall, N. M., & Vourlidas, A. 2015, *The Astrophysical Journal*, 807, 176, doi: [10.1088/0004-637X/807/2/176](https://doi.org/10.1088/0004-637X/807/2/176)
- Virtanen, P., Gommers, R., Oliphant, T. E., et al. 2020, *Nature Methods*, 17, 261, doi: [10.1038/s41592-019-0686-2](https://doi.org/10.1038/s41592-019-0686-2)
- Vourlidas, A., Howard, R. A., Plunkett, S. P., et al. 2016, *Space Science Reviews*, 204, 83, doi: [10.1007/s11214-014-0114-y](https://doi.org/10.1007/s11214-014-0114-y)
- Wexler, D., Imamura, T., Efimov, A., et al. 2020, *Solar Physics*, 295, 111, doi: [10.1007/s11207-020-01677-1](https://doi.org/10.1007/s11207-020-01677-1)